Electronic Supplementary Material (ESI) for Journal of Materials Chemistry C.
This journal is © The Royal Society of Chemistry 2019

Electronic Supporting Information for

Luminescent Silver-Lithium-Zeolite Phosphors for Near-Ultraviolet LED Applications

Wouter Baekelant,[1,2] Saleh Aghakhani,[3] Eduard Fron,[1] Cristina Martin,[1,4] Cheol Woong-Kim,[1,5] Julian A. Steele,[2] Trees De Baerdemaeker,[2] Francesco d'Acapito,[6] Dmitry Chernysov,[7] Mark van der Auweraer,[1] Peter Lievens,[3] Didier Grandjean,[3,*] Maarten Roeffaers,[2,*] Johan Hofkens,[1,*] Eduardo Coutino-Gonzalez.[8,*]

[1]Chem&Tech - Molecular Imaging and Photonics, KU Leuven, Celestijnenlaan 200F, B-3001 Leuven, Belgium.

[2]Chem&Tech - Centre for Membrane Separations, Adsorption, Catalysis and Spectroscopy for Sustainable Solutions, KU Leuven, Celestijnenlaan 200F, B-3001 Leuven, Belgium.

[3]Department of Physics and Astronomy, Laboratory of Solid-State Physics and Magnetism, KU Leuven, Celestijnenlaan 200D, B-3001 Leuven, Belgium.

[4]Departamento de Química Física, Facultad de Farmacia, Universidad de Castilla-La Mancha, Campus Universitario, 02071 Albacete, Spain.

[5]Institute for Global Climate Change and Energy, Kyungpook National University, Daegu 41566, Korea.

[6]CNR-IOM-OGG c/o ESRF, LISA CRG, 71 Avenue Des Martyrs, 38043 Grenoble, France.

[7]Swiss–Norwegian Beamlines, ESRF, The European Synchrotron, CS40220, 38043 Grenoble, France.

[8]CONACYT - Centro de Investigación y Desarrollo Tecnológico en Electroquímica, Parque Industrial Querétaro, Sanfandila s/n, Pedro Escobedo 76703, Querétaro, Mexico.

Contents

I. Zeolites characterization

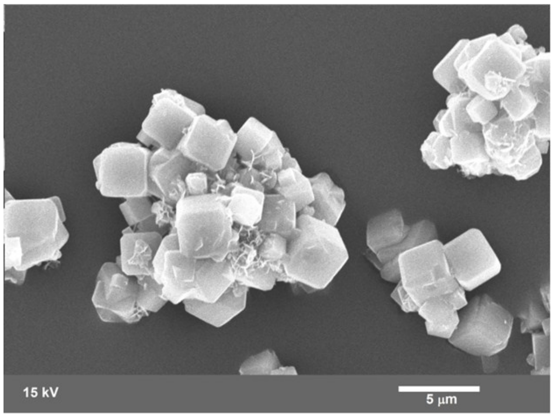

Figure S1. SEM micrographs of the Na-LTA zeolites used in this study. The images were recorded on a JEOL-6010LV SEM. Typical cubic shapes with truncated edges and a size distribution between 2 to 5 μm are observed.

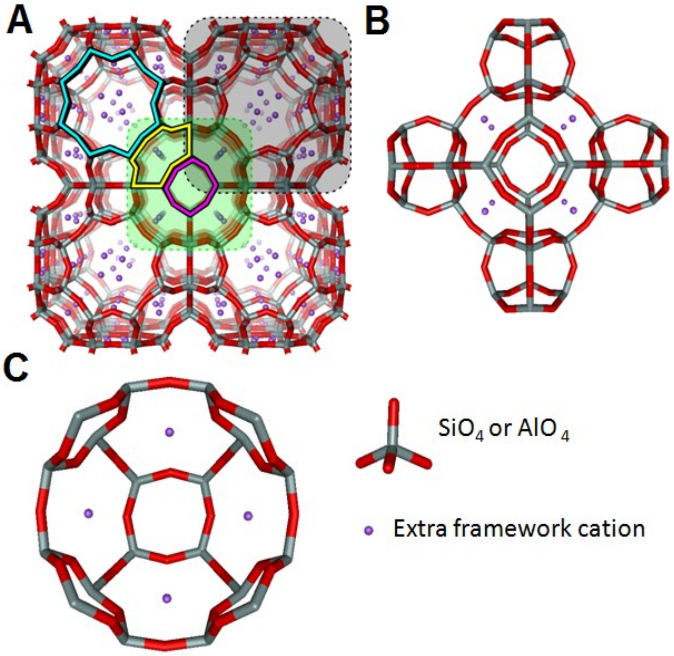

Figure S2. Schematic representation of A) LTA unit cell displaying the sodalites (green dashed area) and super cages (gray dashed area); the single eight-membered rings (S8Rs), single six-membered rings (S6Rs), and single four-membered rings (S4R) are highlighted in cyan, yellow and pink, respectively, B) isolated sodalite cage showing the S4R connectors, and C) transversal section of a sodalite cage.

II. Used devices

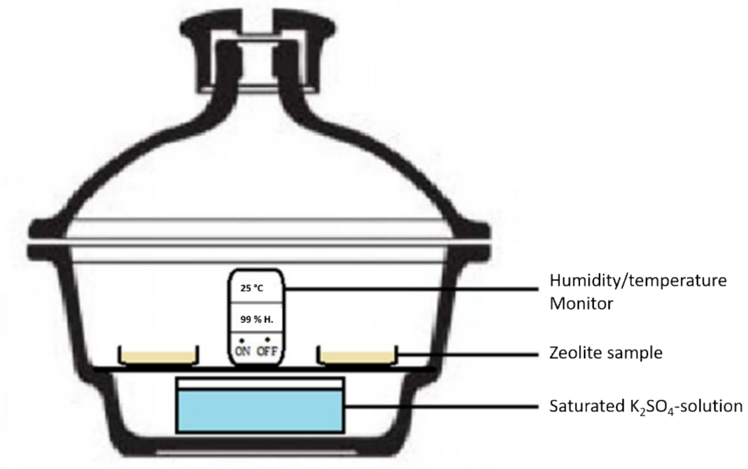

Figure S3. Closed container having a relative humidity of 99% used for the controlled hydration of the Ag_1 Li-LTA sample.

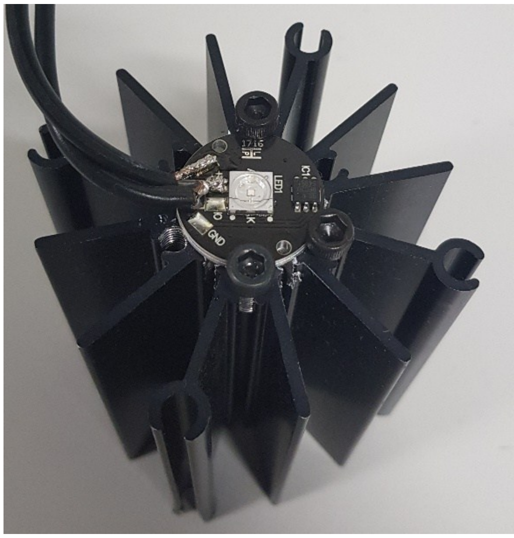

Figure S4. 340 nm NUV-LED used in this study.

III. Elemental analysis

The elemental analysis of the Li^+-exchanged sample was performed by digesting the zeolite sample in a HF/aqua regia solution. Afterwards the elemental composition of Na and Li was determined using an atomic absorption spectroscopy (AAS). The results are displayed in the table below.

Table S1. Elemental composition of Li-Exchanged zeolite. The sample for ICP-MS analysis were 4 times more diluted compared to AAS samples.

Name	Weight (g)	Result (ppm)	Conc. in vol. Flask (ppm)	mg/50ml	mg/100ml wt%	Average Wt%	Molar comp.	Elemental comp. #CBI=12*
Li	0.0573	2.6195	26.195	2.6195	4.57	4.52	0.659	11.98
	0.0505	2.2543	22.543	2.2543	4.46			
Na	0.051	0.02478	0.248	0.0124	0.0243		0.00106	0.02
Si	0.051	40	220.912	11.0456	21.66		0.771	14.03
Al	0.051	40	180.896	9.0448	17.73		0.657	11.96

*#CBI: number of counterbalancing ions

From the results we can determine that 99.8 % (=0.659/(0.659+0.00106)) of the original Na counterbalancing ions are replaced by Li^+ during the exchange procedure.

IV. Characterization of the optical properties of commercial zeolites

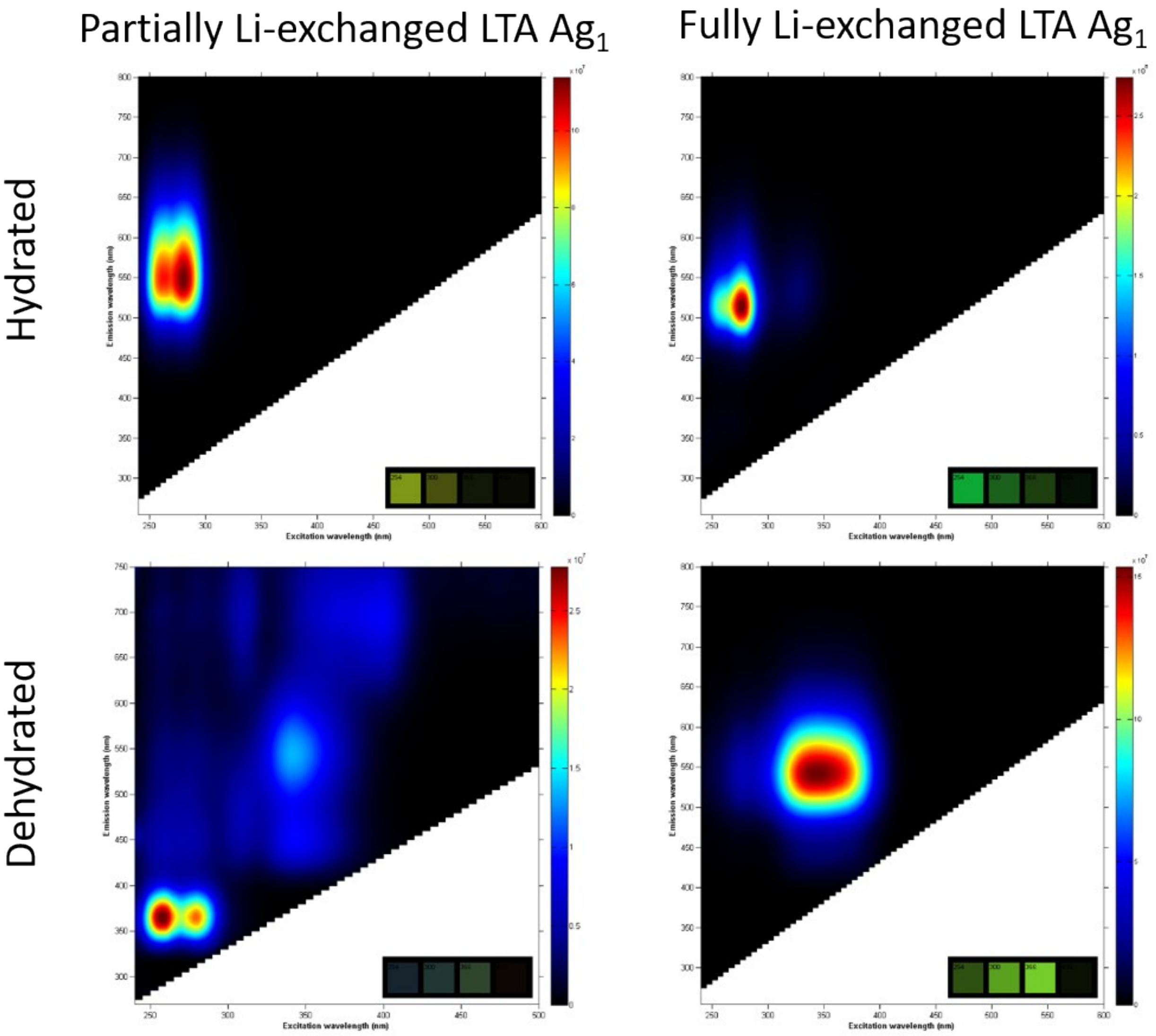

Figure S5. The luminescent properties of Ag_1-exchanged fully (left) and partially (right) Li-exchanged LTA zeolites in both hydrated (top) and dehydrated (bottom) state.

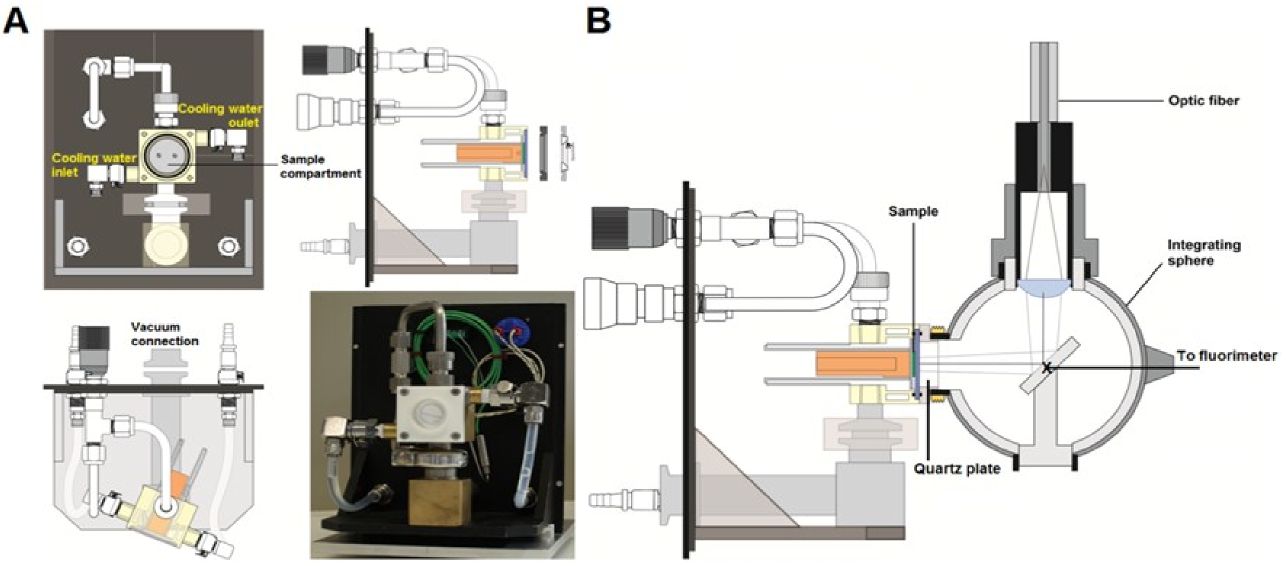

Figure S6. Schematic representation of the in-house spectroscopic-compatible cell. (A). Front, side, top & real view of the spectroscopic-compatible cell employed in this study. (B). Side view of the spectroscopic-compatible cell attached to the integrating sphere.

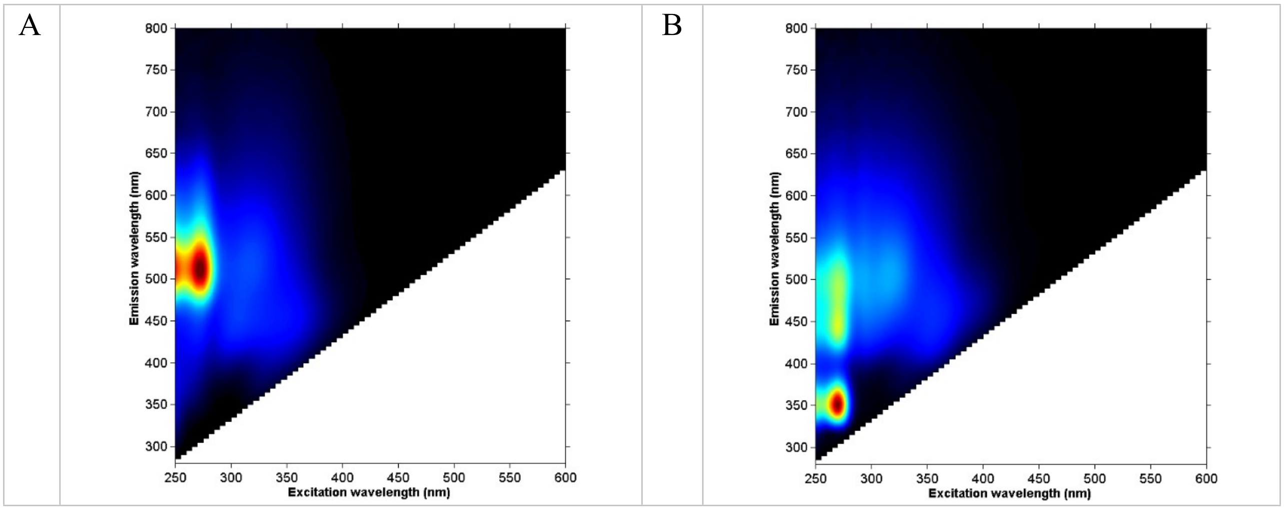

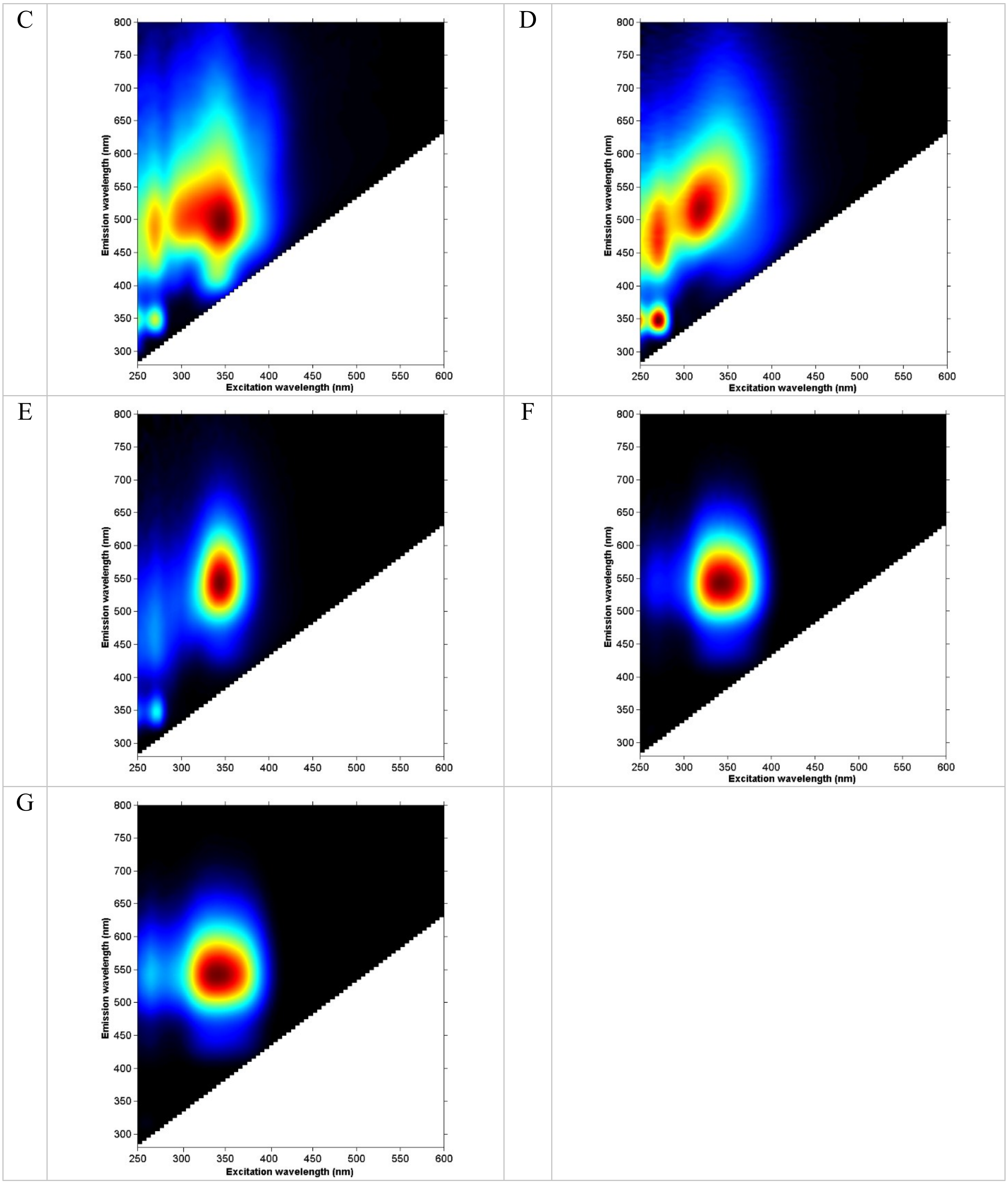

Figure S7. 2D excitation/emission plot of Ag$_1$ Li-LTA at different dehydration temperature: (A) Room temperature, (B) 100 °C, (C) 200 °C, (D) 300 °C, (E) 350 °C, (F) 400 °C, (G) 450 °C.

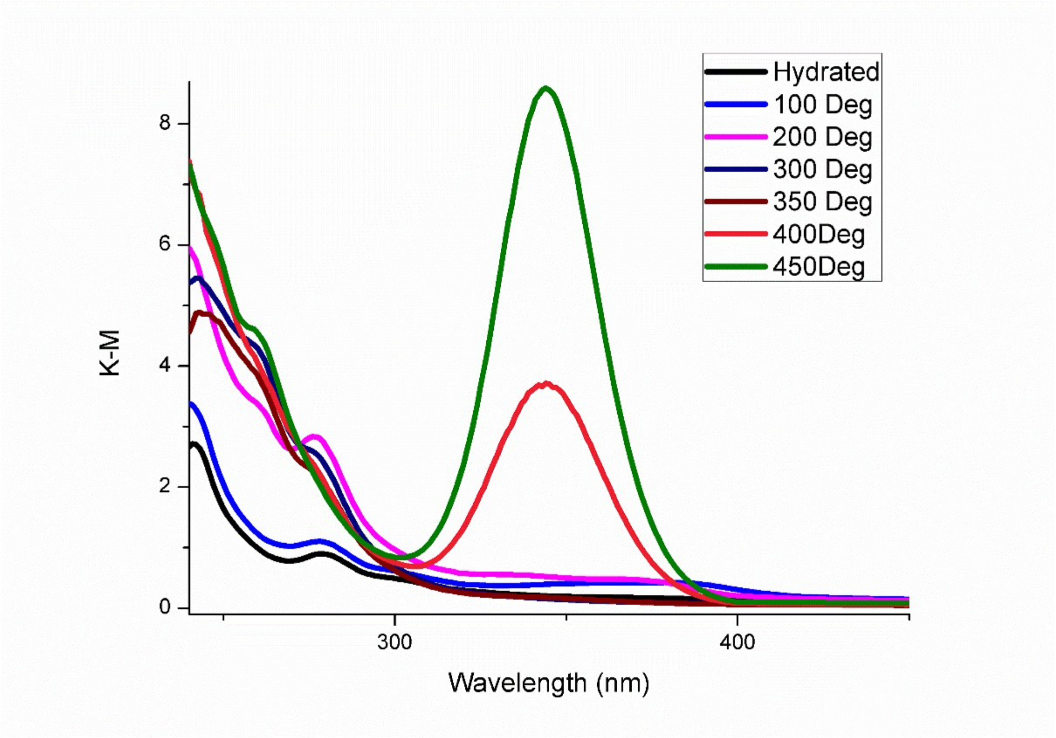

Figure S8. Kubelka-Munk converted DRS spectra of the Ag_1 Li-LTA sample at different hydration levels.

V. EXAFS analysis

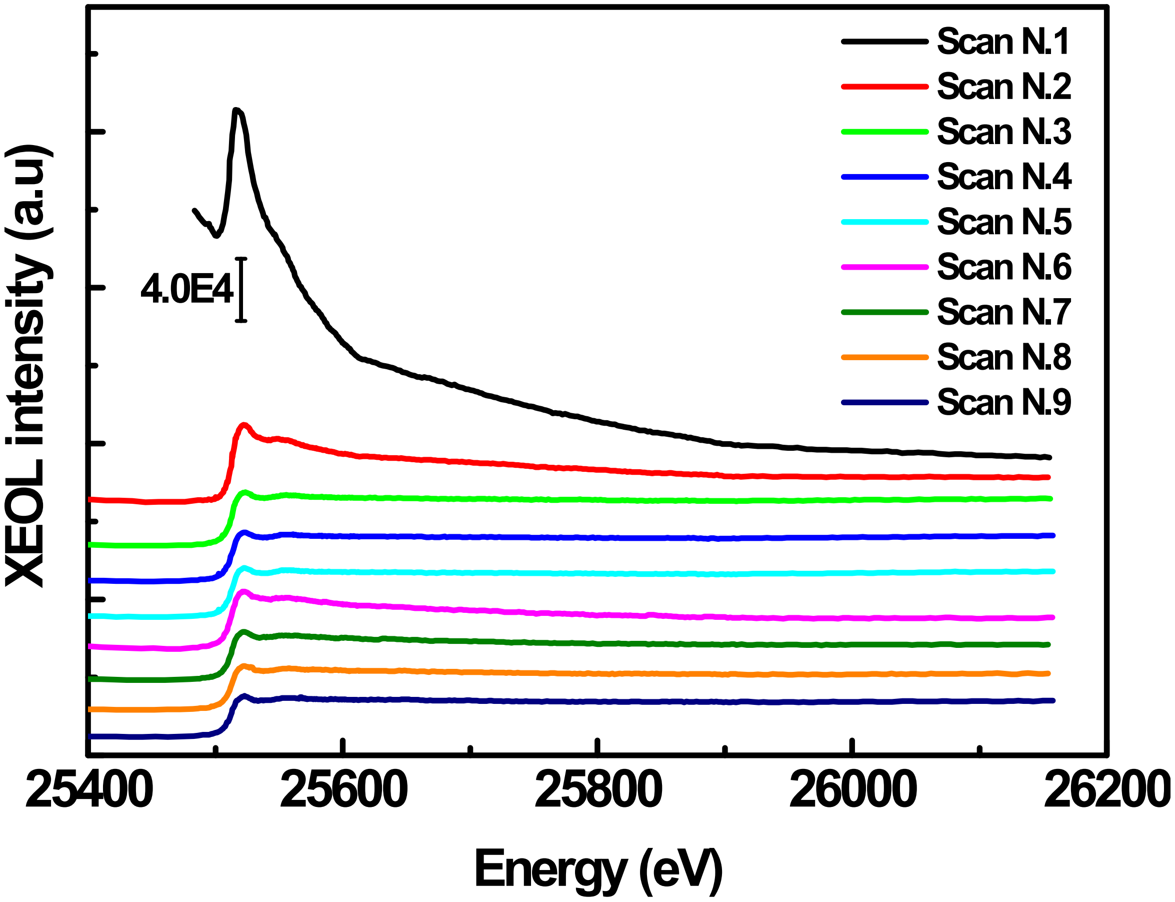

Figure S9. Variation of XEOL-EXAFS spectra intensity for each separate scan.

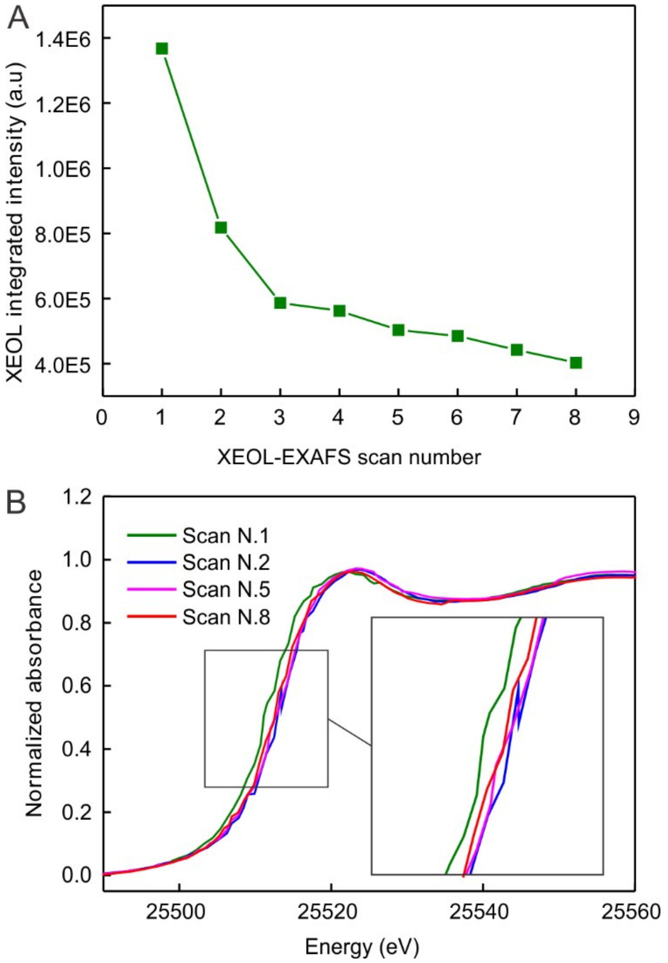

Figure S10. (A) Integrated intensity of the XEOL-EXAFS spectra for the dehydrated Ag_1Li_{11}-LTA sample and (B) Tr-XANES spectra of the different scans for this sample. The inset shows a zoom-in of the edge position of the different scans of the dehydrated Ag_1Li_{11}-LTA sample.

EXAFS structural characterization

Sodalite cages are composed of 8 single six-membered rings (S6Rs) and 6 single four-membered rings (S4Rs) which are connected through double four-membered rings (D4Rs) forming a super cage (see Figure S2). Detailed EXAFS fittings of AgCLs in Li-LTA zeolites were discussed in our previous works. [3,4] Therefore, the structural results will only be briefly discussed. To fit the EXAFS data, we used a structural model based on a combination of Ag-O, Ag-Ag, Ag-Li, Ag-Si/Al shells with a virtual mixed Si/Al site corresponding to a 50% Si:50% Al occupancy to reflects better the Si/Al = 1 of LTA zeolites that showed the best agreement to the data in our previous works.

Transmission-EXAFS analysis

The average of scan 1 to 8 transmission-EXAFS (Tr-EXAFS) k^3-weighted $\chi(k)$ and the corresponding phase-corrected Fourier Transform (FT) best fits of Ag_1 Li-LTA dehydrated are presented in Figures 3 A&B and the fitting parameters are listed in Tables 1 and S2. Three pronounced peaks in the 1.5-4.0 Å range are observed in the FT profile. The first peak (N_1) consists of 2.0 O atoms at 2.23 Å corresponding to a combination of framework O atoms (O_F) corresponding to Ag cations occupying the center of the S6Rs ($Ag_{R,}$ Figure S2) as well as to non-framework O atoms (O_{NF}) coordinated to Ag_C forming the clusters (see below). The second multi-peak is composed of an Ag-Si/Al shell (N_4) consisting of 2.4 Si/Al at 3.26 Å. The Ag-Si/Al contributions correspond to the Ag_R atoms that are strongly bonded to three framework oxygen atoms (N_1) pointing towards the center of the S6Rs. In the crystallographic model of fully Ag exchanged LTA zeolites, Ag_R atoms located in the plane of the S6Rs have a Ag_R-Si/Al distance of 3.25 Å[4] in line with the distance obtained by the EXAFS analysis. The corresponding crystallographic Ag_R-O distance is 2.27 Å confirming that the 2.23 Å distance (N_1) is a combination of O_{NF} atoms located at shorter distance. Ag_R atoms are then coordinated to 2.4 Si/Al (N_4) and 1.2 O_F (N_1) implying a 2:1 ratio of the Si/Al and O coordination numbers (CN). The remaining 1.3 O_{NF} atoms (2.0-1.2/0.6) at an estimated distance of 2.20 Å are attributed to the oxygen atoms coordinating AgCLs (see below).

The second multi-peak also includes a short distance Ag-Li contribution of 3.0 (1.8 (N_3)/0.6) Li atoms at 2.71 Å (N_3) that are positioned in the axis of the S4Rs inside the sodalite cage. In addition, a significant Ag-Ag shell (N_2) consisting of 1.5Ag at 2.57 Å (N_2) is required to complete the fitting of the second multi-peak. This contribution corresponds to the remaining part of the Ag atoms forming oligomeric AgCLs (Ag_C) located inside the sodalite cages. A direct calculation indicates that the Ag_R fraction corresponds to 40% (2.4 (N_2)/6, see Table S2) of the total number of the Ag atoms in the dehydrated Ag_1 Li-LTA sample. The fraction of AgCLs is then 60 % and the nuclearity of 2.5 (1.5/0.50) suggest that the clusters nuclearity is a mixture of Ag_3 and Ag_4 clusters. To complete the EXAFS structural model each Ag_C atom is then coordinated to 1.3 O_{NF} atom (2.0-1.2/0.6) that most likely correspond to atomic oxygen atoms that have replaced the water molecules coordinated to the cluster above 350 °C (Figure 3).

The third peak is attributed to long distance Ag-Ag shell of 0.7 Ag at 3.53 Å (N_5). Inspection of the sodalite crystallographic structure suggests that this long Ag-Ag distance corresponds to the distance between Ag_C atoms forming the AgCLs at the center of the sodalite cages and Ag_R atoms occupying the center of the S6Rs (Ag_C-Ag_R). A similar long distance Ag_C-Ag_R shell was observed in Ag exchanged Na- and K-LTA zeolites within the 3.37-3.52 Å range.

To sum up, the Tr-EXAFS results showed that a mixture of $Ag_{3/4}$ clusters faced with~2 O atoms (O_{NF}) close to the center of the S6Rs corresponding in average to $Ag_{3/4}(O_{NF})_2$ structures are formed at the center of the sodalites of dehydrated Ag_1 Li-LTA. These structures are further surrounded by 6 Li cations close to the center of the S4Rs inside the sodalites and 0.7 Ag_{6R} cations residing on the S6Rs (see Figure 4). This local agglomeration of Ag atoms in a limited number of sodalite cages in Ag_1 Li-LTA that contain only a very small number of Ag cations points out a strong concentration of the silver atoms in the zeolite.

XEOL-EXAFS Analysis

k^3 weighted XEOL-EXAFS and corresponding phase-corrected Fourier Transform (FT) best fits are presented in Figures 3 C&D and the fitting parameters are summarized in Tables 1 and S2. As in the Tr-EXAFS results, three peaks in the 1.5-4.0 Å range are observed in the FT. The first intense peak is attributed to 1.5 O atoms at 2.21 Å (N_1) while the second multi-peak corresponds to a combination of 2.0 Ag_C atoms at 2.55 Å (N_2) and 1.8 Li atoms at a distance of 2.70Å (N_3). Finally, a long-range Ag_C-Ag_R shell of 0.8 Ag at 3.59 Å(N_5) was added to complete the structural fitting. The XEOL-EXAFS results indicate that Ag_C atoms are coordinated to nearly 1.5 O atoms (O_{NF}) and 2 Ag_C (N_2) forming an average of $Ag_3(O_{NF})_2$ clusters. These structures are formed in the center of the sodalite cages in which each Ag_C atom is enclosed with 0.8 Ag_R atom (N_4) located in the S6Rs of the same sodalite cage. Ag_C atoms in $Ag_3(O_{NF})_2$ structures are further surrounded at very short distances by 1.8 Li cations corresponding to ca. 4 Li cations located inside the same sodalite and positioned in the axis of the S4Rs, in line with our previous results.

Tr-EXAFS averaged over scan 1 to 8 shows the formation of average $Ag_{3/4}(O_{NF})$ structures while the XEOL-EXAFS averaged over scan 3 to 8 points towards the presence of $Ag_3(O_{NF})_2$ structures with shorter Ag_C-Ag_C distance (2.55 vs. 2.57 Å). This discrepancy suggests that the nuclearity of the most luminescent AgCLs (scan 1) is likely close to 4. This is supported by the XEOL-XANES analysis (Figure 2B) showing the specific profile of scan 1 spectrum compared to those of the following scans suggesting the transformation of the different AgCLs structure. This is further confirmed by the analysis of XAFS of each individual scan that are discussed in the main text.

Table S2. Summary of Ag K-edge EXAFS structural refinements of the dehydrated $Ag_1Li_{12}LTA$ zeolites based on the average XEOL- (scan 2-8, red color) and transmission- (scan 1-8, black color) EXAFS data.

N_i	Shell	CN_i	R_i(Å)	A_i(Å^2)
1	**Ag_{C+R} -O**	1.5(2) 2.0(3)	2.21(2) 2.23(2)	0.025(3) 0.031(3)
2	**Ag_c-Ag_c**	2.0(4) 1.5(5)	2.55(3) 2.57(4)	0.029(3) 0.024(4)
3	**Ag_c-Li**	1.8(4) 1.8(4)	2.70(3) 2.71(4)	0.010(3) 0.008(2)
4	**Ag_R-(Si/Al)**	- 2.4(5)	- 3.26(4)	- 0.050(4)
5	**Ag_c-Ag_R**	0.8(3) 0.7(3)	3.59(4) 3.53(4)	0.025(3) 0.012(3)

N_i: Shell number, **CN_i:** Coordination number of atom in the N_ith shell, **R_i:** Radial distance of atoms in the N_ith shell [Å], **A_i**: Debye-Waller term of the N_ith shell ($A=2\sigma^2$ with σ^2= Debye-Waller factor)[Å^2], **R*:** Error factor (%) **Ag_C**: Ag atom composed of Ag cluster, Ag_R: Ag cation coordinated with the S6Rs, **Ag_c:Ag_R** is a percentage of Ag_c and Ag_R fraction in each EXAFS model, **E_F** is contribution of the wave vector of the zero photoelectron relative to the origin of k [eV]. **AFAC** is an amplitude reduction due to many-electron processes that was fixed to 0.9 after calibration with an Ag foil.

VI. Single crystal XRD analysis

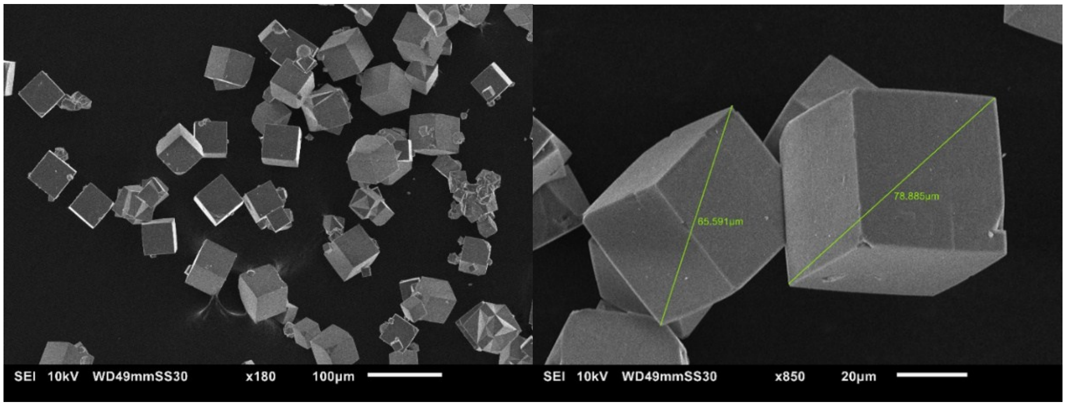

Figure S11. SEM image of single crystal used for single crystal XRD analysis.

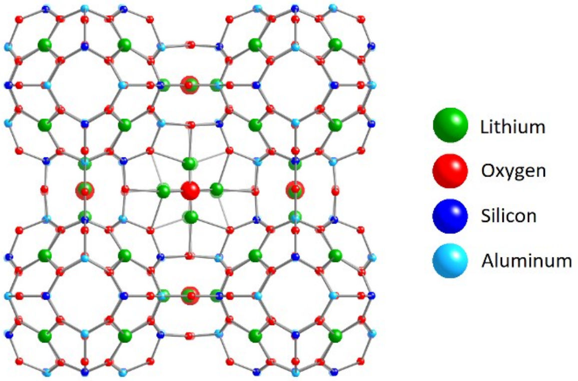

Figure S12. Single-crystal structures of dehydrated Li-LTA with all non-framework positions (Li and non-framework oxygen) including symmetry equivalents.

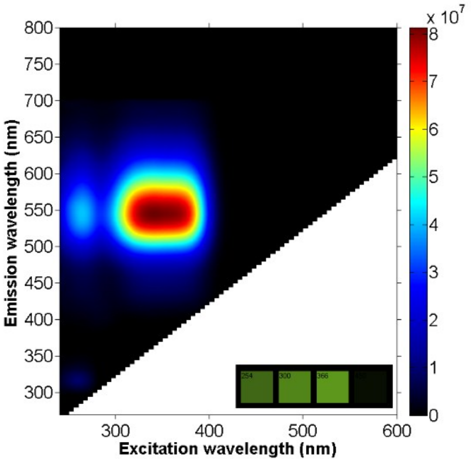

Figure S13. Photoluminescence properties of dehydrated Ag_1 Li-LTA-SC zeolites.

Table S3. Lattice parameters of the unit cell of the different Ag-exchanged LTA zeolites depending on the counterbalancing ions and hydration level using PXRD.

Sample	**Lattice parameters – unit cell PXRD**	
	Hydrated	Dehydrated
Na-LTA	24.5679(3) Å$^{(1)}$	24.5613(2) Å$^{(2)}$
Ag_1 Na-LTA	24.5788(7) Å$^{(1)}$	24.5460(2) Å$^{(2)}$
Li-LTA	24.0232(8) Å$^{(2)}$	23.9058(9) Å$^{(1)}$
Ag_1 Li-LTA	24.0290(5) Å$^{(2)}$	23.8962(3) Å$^{(2)}$

Table S4.

	Li-LTA
crystal cross-section (mm)	0.07
X-ray source	ESRF(SNBL-BM01A)[a]
wavelength (Å)	0.7231
Detector	PILATUS 2M
crystal-to-detector distance (mm)	150
detector vertical position (mm)	80
data collection temperature (T (K))	294(1)
space group, No.	$Fm\bar{3}c$, 226
unit cell constant, a (Å)	23.9080(2)
maximum 2θ for data collection (deg)	63.97
no. of reflections measured	98713
no. of unique reflections measured, m	1005
no. of reflections with $F_o > 4\sigma(F_o)$	955
no. of variables, s	46
data/parameter ratio, m/s	21.8
weighting parameters: a, b	0.0402, 26.167
final error indices: R_1[b], R_2[c]	0.029, 0.091
goodness of fit[d]	1.27

Experimental and Crystallographic Data of Li-LTA and Ag1 Li-LTA single crystals.

[a]Swiss-Norwegian Beamline (SNBL) BM01A at the European Synchrotron Radiation Facility, France. [b]$R_1 = \Sigma|F_o - |F_c||/\Sigma F_o$; R_1 is calculated using only those reflections for which $F_o > 4\sigma(F_o)$. [c]$R_2 = [\Sigma w(F_o^2 - F_c^2)^2/\Sigma w(F_o^2)^2]^{1/2}$ is calculated using all unique reflections measured. [d]Goodness of fit = $(\Sigma w(F_o^2 - F_c^2)^2/(m - s))^{1/2}$.

Table S5. Positional, Thermal, and Occupancy Parameters[a]

atom position	Wyckoff position	x	y	z	U_{11} or U_{iso}[b]	U_{22}	U_{33}	U_{23}	U_{13}	U_{12}	occupancy[c]	
											varied	fixed
					Li-LTA							
Si	96(i)	0[d]	9228(2)	18024(2)	149(2)	142(2)	107(2)	15(1)	0[d]	0[d]		96
Al	96(i)	0[d]	18268(2)	8897(2)	152(2)	107(3)	153(3)	14(2)	0[d]	0[d]		96
O1	96(i)	0[d]	9535(6)	24663(5)	229(6)	365(8)	118(5)	21(5)	0[d]	0[d]		96
O2	96(i)	0[d]	15514(5)	15597(5)	259(6)	157(6)	169(6)	22(4)	0[d]	0[d]		96
O3	192(j)	5551(4)	6015(4)	15708(4)	186(4)	193(4)	171(4)	29(3)	31(3)	41(4)		192
Li1	64(g)	9493(13)	9493(13)	9493(13)	292(10)	292(10)	292(10)	115(12)	115(12)	115(12)	66.8(16)	64
Li2	96(i)	0[d]	18678(69)	25312(88)	613(109)	349(75)	949(151)	24(78)	0[d]	0[d]	42.4(30)	32
O4	24(d)	0[d]	25000[d]	25000[d]	1314(70)	869(31)	869(31)	0[d]	0[d]	0[d]	24.0(5)	24

[a] Positional parameters × 10^5 and thermal parameters × 10^4 are given. Numbers in parentheses are the estimated standard deviations (esds) in the units of the least significant figure given for the corresponding parameter. [b] The anisotropic temperature factor is $\exp[-2\pi^2 a^{-2}(U_{11}h^2 + U_{22}k^2 + U_{33}l^2 + 2U_{12}hk + 2U_{13}hl + 2U_{23}kl)]$. [c] Occupancy factors are given as the number of atoms or ions per unit cell. [d] Exactly, by symmetry.

Table S6. Selected Interatomic Distances (Å) and Angles (deg)[a]

Distances		Angles	
Si–O1	1.5890(13)	O1–Si–O2	108.46(8)
Si–O2	1.6109(13)	O1–Si–O3	111.16(4)
Si–O3	1.6302(9), 1.6303(9)	O2–Si–O3	108.50(4)
mean	1.6151	O3–Si–O3	108.99(7)
		mean	109.28[b]
Al–O1	1.6970(13)		
Al–O2	1.7319(13)	O1–Al–O2	107.18(7)
Al–O3	1.7557(9)	O1–Al–O3	112.84(4)
mean	1.7282	O2–Al–O3	106.79(4)
		O3–Al–O3	109.99(7)
		mean	109.20[b]
Li1–O3	1.9462(10)		
		Si–O1–Al	172.20(11)
Li2–O1	2.191(17)	Si–O2–Al	133.45(8)
Li2–O2	2.314(20), 2.443(21)	Si–O3–Al	129.68(6)
		mean	145.11
Ag1–O2		O3–Li1–O3	119.28(5)
Ag1–O1			
		O1–Li2–O2	75.5(6), 67.9(5)
		O2–Li2–O2	143.4(8)
		O2–Ag1–O2	
		O1–Ag1–O2	
O4···O2	3.1933(13)	O2···O4···O2	90[c], 180[c]
O4···O1	3.6983(15)		

[a] The numbers in parentheses are the estimated standard deviations (esds) in the units of the least significant digit given for the corresponding value. [b] Very nearly the tetrahedral angle, 109.47°. [c] Exactly by symmetry.

VII. Photoluminescence properties at cryogenic temperatures

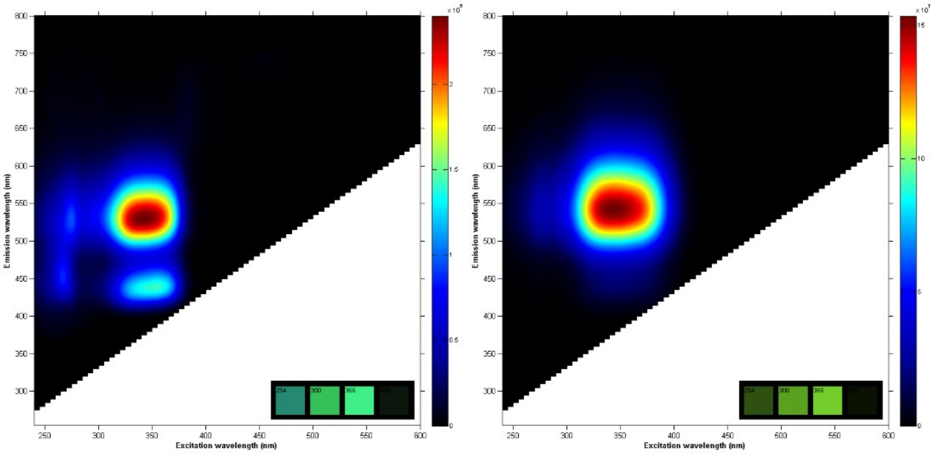

Figure S14. 2D excitation emission plot of Ag_1 Li-LTA at 77K (left) and at room temperature (right).

Spectral analysis of Ag_1 Li-LTA was performed by converting the spectrum to intensity versus wavenumber and fitting the spectra with multiple Gaussian peaks.

Table S7. Emission peaks at the different excitation maxima for Ag_1 Li-LTA both RT and 77K.

RT	Emission spectra		
	@265 nm	@335 nm	@370 nm
	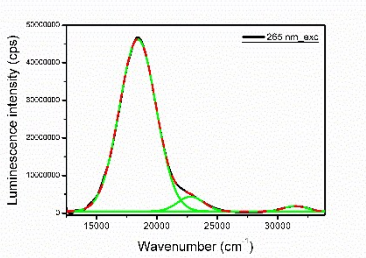	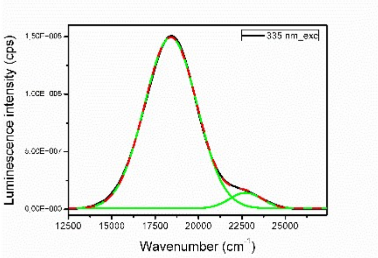	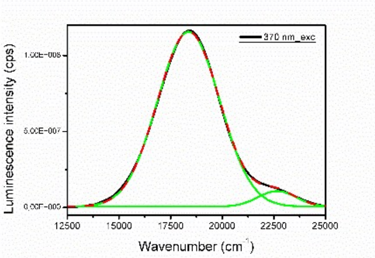
	R^2 = 0,99951	R^2 = 0,99951	R^2 = 0,99955
	Excitation spectra		
	@320 nm	@440 nm	@ 545 nm
	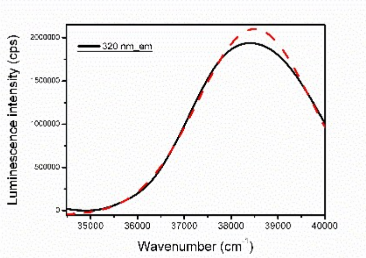	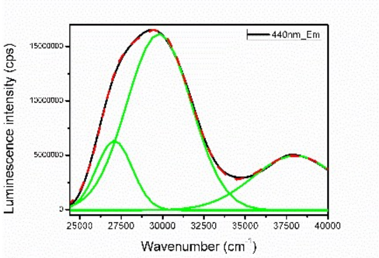	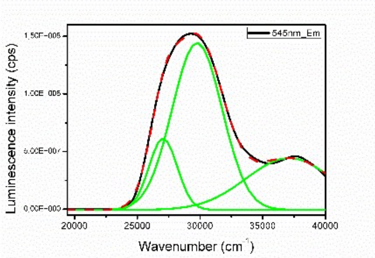
	R^2 = 0,98828	R^2 = 0,99953	R^2 = 0,99931
77 K	Emission spectra		
	@270 nm	@335 nm	@360 nm

	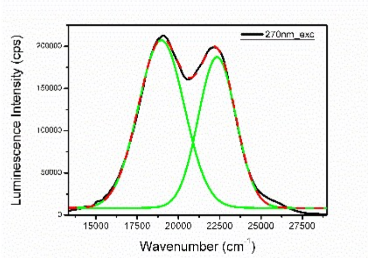	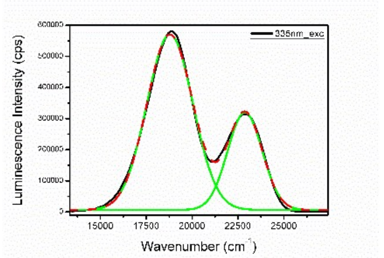	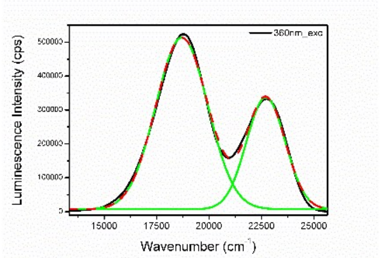
	R^2 = 0,99835	R^2 = 0,99749	R^2 = 0,99721
	Excitation spectra		
		@440 nm	@ 530 nm
		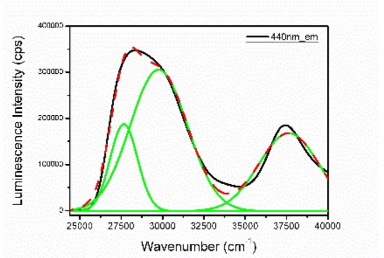	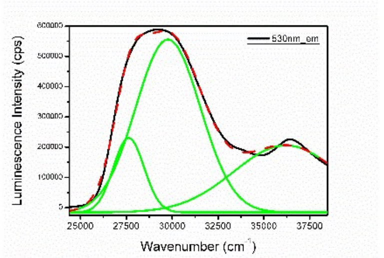
		R^2 = 0,99199	R^2 = 0,99661

Table S8. Emission peaks at the different excitation maxima for Ag_1 Li-LTA both RT and 77K.

Room temperature					77 K				
λ_{exc} (nm)	λ_{em} (nm)	$FWHM_{exc}$ (cm^{-1})	$FWHM_{em}$ (cm^{-1})	I*	λ_{exc} (nm)	λ_{em} (nm)	$FWHM_{exc}$ (cm^{-1})	$FWHM_{em}$ (cm^{-1})	I*
265	320	526315	120481	1.23	270				
	440	238095	109890	3.06		440	344827	188679	31.0
	545	166666	126582	30.9		530	196078	108695	37.0
335	440	192307	238095	10.2	335	440	217391	238095	54.9
	545	188679	94339	100		530	212765	119047	100
370	440	285714	232558	5.69	360	440	434782	238095	46.4
	545	277777	94339	60.3		530	400000	119047	66.8

**Normalized average of (Intensity excitation; Intensity Emission)*

VIII. Decay times at cryogenic temperatures

The relatively long decay time of the major emitting state motivated further examination at cryogenic temperatures (Figure S13, Table S7, S8). Besides a small blue shift of the main emission band to 530 nm, we observed an increase of the 480 nm emission. The 2D excitation-emission spectra obtained at 77 K (Figure S13) clearly indicate that the blue (480 nm) and green (530 nm) emission involve the same initially excited Franck Condon state. The luminescence decay experiments showed slower decays of 25 ns and 325 μs (Figure S14). The 325 μs species feature again a Gaussian-like distribution of its amplitude-to-wavelength dependence, with a maximum that is blue shifted (530 nm) compared to the one at RT. As expected, this spectral dependence resembles the steady-state emission recorded at 77 K. The fact that, except a small blue shift and a small increase in lifetime, the kinetics changes very little between room temperature and 77 K (in contrast to the hydrated silver-exchanged sodium LTA samples)[5] pointing to a well-defined species, i.e. the triplet excited state of an $Ag_4(O_{NF})_2$-$[Li^+]_6$ cluster. Such species is responsible for the long-lived emission and a relatively simple kinetic scheme, in comparison to previous reports.[5] The blue shift suggest a less complete relaxation of the environment of AgCLs after excitation at 77 K. Considering the high luminescence quantum yield at room temperature, the 50 % increase of the decay means that the radiative rate constant has become at least 20 % smaller at 77 K. This accounts for a less important spin orbit coupling at 77 K. One reason could be the small difference in the geometry of the relaxed excited state of the clusters, the latter being also reflected in the small blue shift of the emission spectrum. The 25 ns species has a similar wavelength maximum at 480 nm accompanied by a low-energy shoulder (now positioned at 600 nm). The absence of any qualitative change of the ns emission upon cooling at 77 K (neither in complexity of the decay nor in the spectral properties of the emission) suggests again a simple kinetic scheme where the 25 ns species is an intermediate, probably a relaxed singlet excited AgCLs. The modest increase in decay time of this ns species upon cooling would correspond to a small decrease of its main decay channel. In view of the large emission quantum yield of the µs species, this decay channel is the conversion of the ns to µs species. When we attributed this ns species to the relaxed singlet state, this process would be an intersystem crossing, which generally has a modest temperature dependence.[6,7]

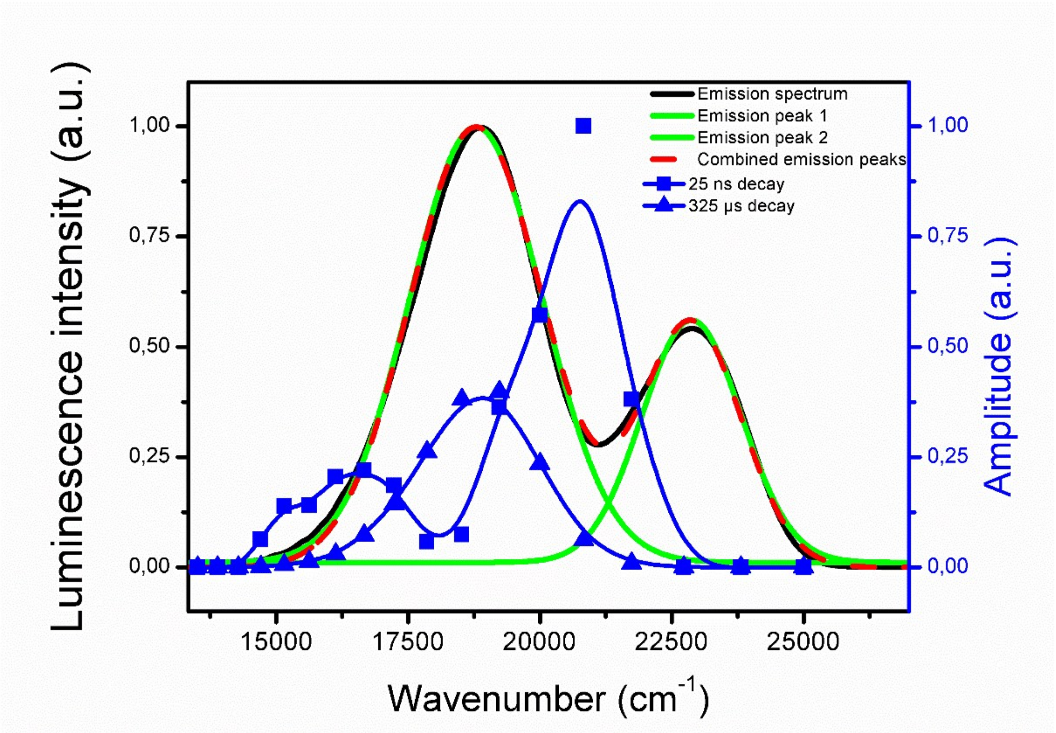

Figure S15. The steady-state emission spectrum at 77K of the dehydrated Ag_1 Li-LTA sample at 335 nm excitation (black), its spectral analysis (green) into different Gaussian emission peaks and the sum of the Gaussian emission peaks (dashed red). In combination with the decay associated spectra (blue) of the different decay times (25 ns and 325 µs) when excited with 355 nm UV-light.

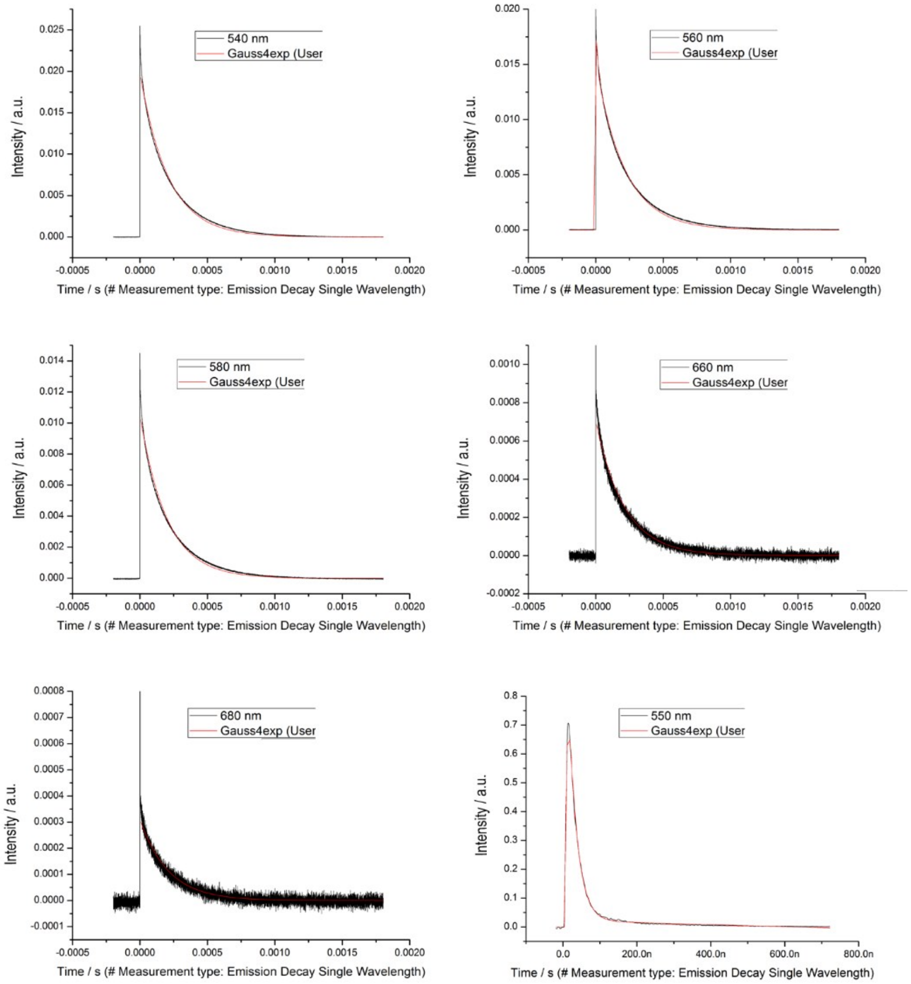

Figure S16. Decay traces of the dehydrated Ag_1 Li-LTA sample obtained in 2 ms time window at room temperature.

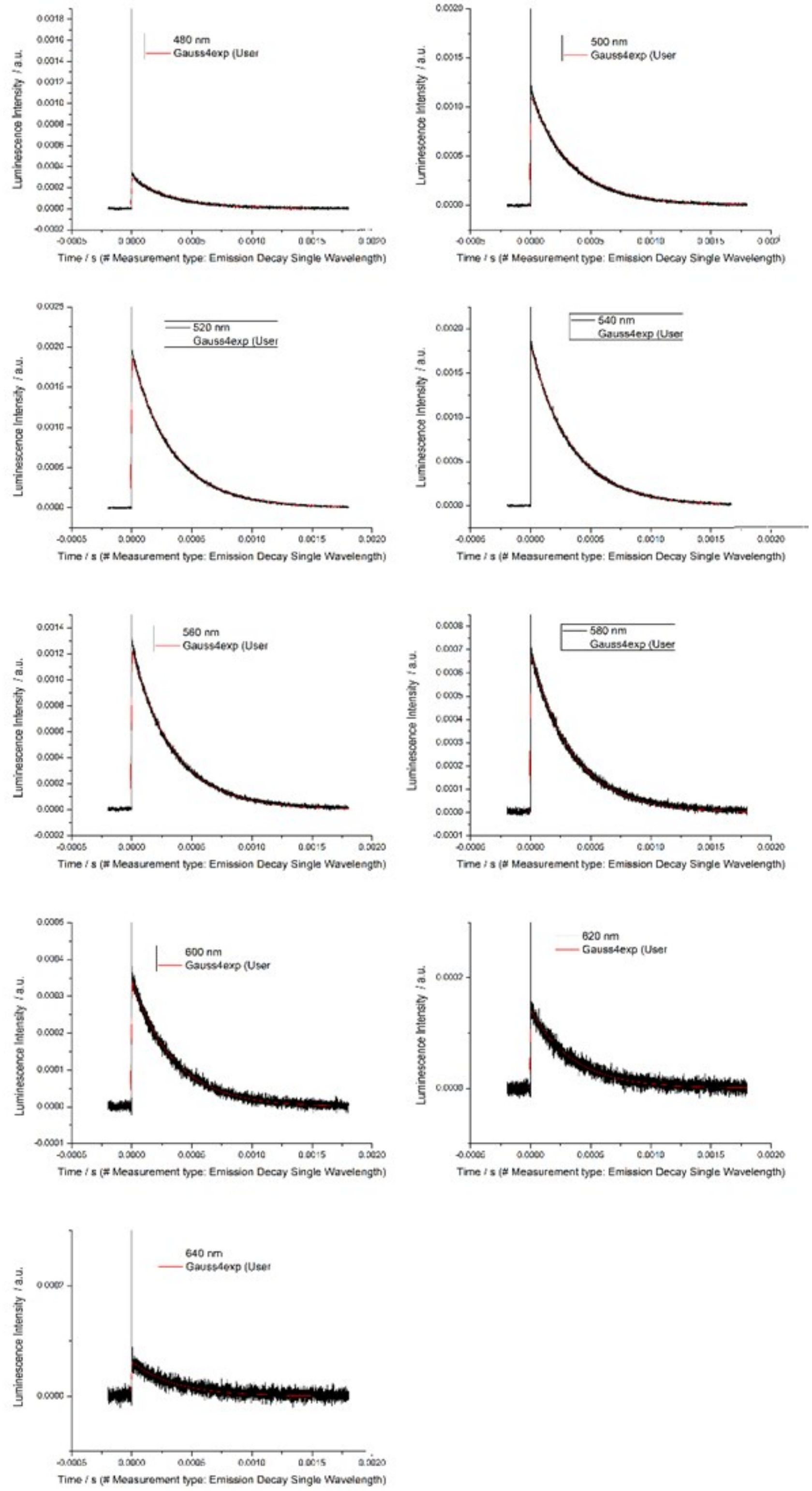

Figure S17. Decay traces of the dehydrated Ag_1 Li-LTA sample obtained in 2 ms time window at 77 K.

IX. References

[1] Fenwick, O.; Coutino-Gonzalez, E.; Grandjean, D.; Baekelant, W.; Richard, F.; Bonacchi, S.; De Vos, D.; Lievens, P.; Roeffaers, M.; Hofkens, J.; Samorì, P. *Nat. Mater.* **2016**, *15*, 1017–1022.

[2] Coutino-Gonzalez, E.; Baekelant, W.; Grandjean, D.; Roeffaers, M. B. J.; Fron, E.; Aghakhani, M. S.; Bovet, N.; Van der Auweraer, M.; Lievens, P.; Vosch, T.; Sels, B.; Hofkens, J. *J. Mater. Chem. C* **2015**, *3*, 11857–11867.

[3] Grandjean, D.; Coutino-Gonzalez, E.; Cuong, N. T.; Fron, E.; Baekelant, W.; Aghakhani, S.; Schlexer, P.; D'Acapito, F.; Banejeree, D.; Roeffaers, M. B. J.; Nguyen, M. T.; Hofkens, J.; Lievens, P. *Science* **2018**, *361*, 686–690.

[4] Aghakhani, S.; Grandjean, D.; Baekelant, W.; Coutino-Gonzalez, E.; Fron, E.; Kvashnina, K.; Roeffaers, M. B. J.; Hofkens, J.; Sels, B. F.; Lievens, P. *Nanoscale* **2018**, *10*, 11467–11476.

[5] Fron, E.; Aghakhani, S.; Baekelant, W.; Grandjean, D.; Coutino-Gonzalez, E.; Van der Auweraer, M.; Roeffaers, M.B.J.; Lievens, P.; Hofkens, J. Structural and Photophysical Characterization of Ag Clusters in LTA Zeolites. *J. Phys. Chem. C* **2019**, *123*, 10630-10638.

[6] Henry, B. R.; Siebrand, W. Spin-Orbit Coupling in Aromatic, Hydrocarbons. Analysis of Nonradiative Transitions Between Singlet, and Triplet States in Benzene and Naphthalene. *J. Chem. Phys.* **1971**, *54*, 1072−1085.

[7] T.J. Penfold, E. Gindensperger, C. Daniel, C.M. Marian, Spin-Vibronic Mechanism for Intersystem Crossing, *Chem. Rev.* **2018**, *118*, 6975-7025.